TITLE
ASP Conference Series, Vol. **VOLUME***, **YEAR OF PUBLICATION**
NAMES OF EDITORS

Evolution of massive and magnetized protoplanetary disks

Sébastien Fromang, Caroline Terquem,

Institut d'Astrophysique de Paris, 98Bis Bd Arago,75014 Paris

Steve A. Balbus [1] & Jean-Pierre De Villiers

Virginia Institute of Theoretical Astronomy, Department of Astronomy, University of Virginia, Charlottesville, VA 22903-0818

Abstract. We present global 2D and 3D simulations of self-gravitating magnetized tori. We used the 2D calculations to demonstrate that the properties of the MRI are not affected by the presence of self-gravity: MHD turbulence and enhanced angular momentum transport follow the linear growth of the instability. In 3D, we have studied the interaction between an $m = 2$ gravitational instability and MHD turbulence. We found its strength to be significantly decreased by the presence of the latter, showing that both instabilities strongly interact in their non-linear phases. We discuss the consequences of these results.

1. Introduction

In the early phases of star formation, the forming accretion disks are likely to be very massive because of a strong infall from the parent molecular cloud. These massive disks are subject to the development of gravitational instabilities which transport angular momentum outward (Laughlin, Korchagin, & Adams 1998). In addition, when sufficiently ionized, the disks are also unstable to the MRI (Balbus & Hawley 1991, 1998). The simultaneous development of these instabilities in disks may significantly affect their evolution. We have undertaken a study of self-gravitating magnetized tori by means of numerical simulations.

In section 2, we describe the numerical methods we have used. In section 3, we present the results of the 2D simulations, focusing on the properties of the MRI in a self-gravitating environment. In section 4, we review preliminary results obtained in 3D calculations, and we discuss the implications of our results in section 5.

[1]Laboratoire de Radioastronomie, École Normale Supérieure, 24 rue Lhomond, 75231 Paris CEDEX 05, France

2. Numerical methods

We used the code Zeus-2D (Stone & Norman 1992a, 1992b) to perform the 2D calculations and the code GLOBAL (Hawley & Stone 1995) for the 3D simulations. Both codes solve the MHD equations using time-explicit Eulerian finite differencing and the Constrained Transport method to evolve the magnetic field. The Poisson solver used to calculate the gravitational potential Φ_g involves two steps: we first calculate Φ_g on the boundary, using the Legendre functions well-suited to the cylindrical geometry (Cohl 1999), and we apply the Successive Over-Relaxation method to update Φ_g everywhere on the grid (Hirsch 1988).

3. 2D simulations

We have built an initial equilibrium structure using the Self–Consistent Field (SCF) method (Hachisu 1986). The inner and outer radii of the torus are $R_{in} = 0.3$ and $R_{out} = 1$ respectively. We set the angular velocity $\Omega \propto r^{-1.68}$, where r is the cylindrical radius. A central mass having half the mass of the disk is present. The equation of state is adiabatic.

In the following, we compare the evolution of this torus to its zero mass counterpart, the gravitational potential of the latter being only that of a central point mass. At the beginning of the simulation, a weak poloidal magnetic field is added to the equilibrium structure, with the toroidal component of the vector potential being:

$$A_\phi \propto \rho \cos\left(2\pi \frac{r - R_{in}}{R_{out} - R_{in}}\right) \tag{1}$$

where ρ is the mass density. The components of the magnetic field are then scaled such that the volume averaged ratio of gas to magnetic pressure (hereafter called $\langle\beta\rangle$) equals 1500 for the self-gravitating model and 200 for the zero mass one. The resolution in both model is $(N_r, N_z) = (256, 256)$ in the radial and vertical directions, respectively.

We found the MRI grows in both models, developing approximately the same Maxwell stress (defined by $T_{r\phi}^{Max} = -B_r B_\phi / 4\pi$). In the self-gravitating case, the evolution is very similar to what was found in previous non self–gravitating calculations (e.g. Hawley [2000)]. Namely, the initial linear growth of the instability is followed by a turbulent phase during which angular momentum is transported outward. Turbulence then gradually decays because of the anti-dynamo theorem.

We show in figure 1 the logarithm of the density field in the $(r - z)$ plane during the turbulent phase for both models. In the self-gravitating case (*left panel*), the initial torus has developed a two-component structure, composed of an inner thin disk fed by an outer thick, massive torus. Figure 2 shows the angular momentum l radial profile in the equatorial plane during this phase (*solid line*). As shown by the dashed line, the inner disk is in Keplerian rotation around the central mass. The dotted line is a fit of the outer part of the disk with a power law dependence $l \propto r^{0.9}$, very close to the Mestel profile $l \propto r$.

Coming back to figure 1, the comparison between both models is striking: although the Maxwell stress is similar in the two cases, the self-gravitating torus

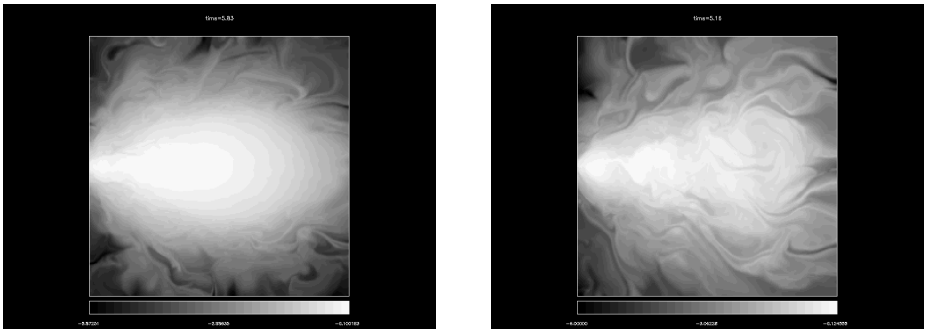

Figure 1. Comparison between the logarithm of the density in the (r-z) plane for the self-gravitating torus (*left panel*) and the zero mass torus (*right panel*). The former develops a two-component structure composed of an inner Keplerian disks and an outer, more massive, thick disk. The later is disrupted by the MRI, and a standard thin disk structure builds up, with a constant H/R ratio.

presents a much more featureless structure than its zero mass counterpart. This result is due to the large scale coherence of the self-gravitating potential, which smoothes MRI fluctuations. We shall see that this effect persists in 3D.

4. 3D simulations

In this section, we present the results of our 3D simulations. As above, we have used the SCF method to compute the disk model, but with different parameters. Here the central mass is twice that of the disk, and the specific angular momentum l in the disk is chosen such that

$$l \propto m^2(r)\,, \tag{2}$$

where $m(r)$ is the mass inside the radius r divided by the total disk mass. The density contours of this disk model are shown in figure 3 (left panel). We introduce the Toomre parameter Q defined by:

$$Q = \frac{c_s \kappa}{\pi G \Sigma}\,, \tag{3}$$

where c_s is the sound speed, κ the epicyclic frequency and Σ the surface density of the disk. Linear studies have shown that a disk becomes gravitationally unstable when Q is of the order of 1. The radial profile of Q in our disk model is shown on the right panel of figure 3. We have $Q \sim 1$ over a large range of radii. We therefore expect the disk to be gravitationally unstable.

4.1. Hydrodynamical simulations

We have performed hydrodynamical simulations to check that our code behaves as expected in this regime. In the simulations presented here, the resolution is $(N_r, N_\phi, N_z) = (128, 64, 64)$ in cylindrical coordinates. The azimuthal domain is restricted to $\phi \in [0, \pi]$, which prevents the growth of modes with odd values

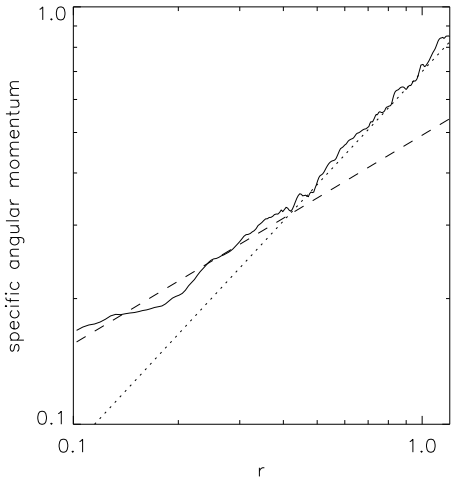

Figure 2. Angular momentum profile in the equatorial plane of the torus, averaged between orbits 5.05 and 7. The dashed line shows the Keplerian profile resulting from the central point mass. The dotted line has a power law dependence with radius: $l \propto r^{0.9}$.

of the azimuthal number m. Time is measured in units of the orbital period at the initial outer edge of the disk.

The time evolution of the Fourier component of the density in the equatorial plane is shown in figure 4 for the modes $m = 2, 4, 6, 8$ (from top to bottom). The $m = 2$ mode grows at the beginning of the simulation and saturates after 4 orbits. The development of this 2 arms spiral structure can be seen on figure 5, which shows the logarithm of the density in the equatorial plane after 4.27 orbits.

During the simulation, matter is driven toward the center of the disk by the gravitational torque associated with the spiral arms. As the surface density in the disk decreases, the Toomre Q parameter increases. As a result, the instability dies away after 8 orbits.

These results are in agreement with earlier simulations of similar disks.

4.2. 3D MHD simulations in an axisymmetric potential

Next, we have performed a 3D MHD calculation of the evolution of the disk in an axisymmetric gravitational potential, i.e. a potential for which we have retained only the $m = 0$ component. This prevents the growth of gravitational instabilities and enables us to check the behavior of our code in the MHD regime. The resolution used for this run is $(N_r, N_\phi, N_z) = (128, 32, 128)$ and the azimuthal domain is $[0, \pi/2]$. A toroidal magnetic field with $\langle\beta\rangle = 8$ is added to the equilibrium model.

The left panel of figure 6 shows the time evolution of the volume averaged Maxwell and Reynolds stress tensors. The Maxwell stress rises during the early part of the evolution (corresponding to the linear development of the instability) before the MRI breaks down into turbulence after 4 orbits. The Reynolds stress is smaller during the whole simulation. The right panel of figure 6 shows the radial profile of the α parameter (defined as the ratio of the total stress to the

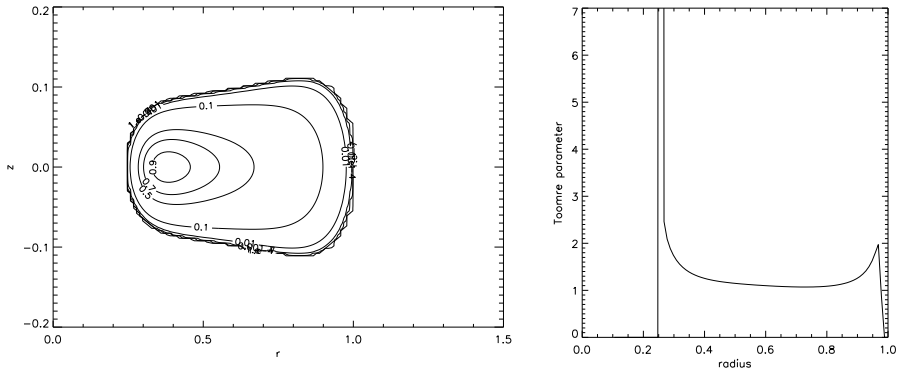

Figure 3. Density contours for the disk model used in the 3D simulations (left panel). The contours shown are $\rho = 10^{-7}, 10^{-4}, 0.001, 0.01, 0.1, 0.5, 0.7$ and 0.9. The right panel shows the radial profile of the Toomre Q parameter.

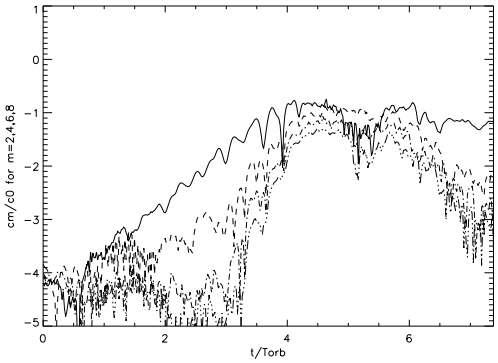

Figure 4. Time evolution of the Fourier components of the density in the equatorial plane for the modes $m = 2, 4, 6, 8$ (from top to bottom). The $m = 2$ mode is unstable.

thermal pressure) at the end of the simulation. It has a typical value of a few times 10^{-2}, similar to values seen in 3D simulations of zero mass disks starting with similar magnetic field configurations (Steinacker & Papaloizou 2002).

4.3. Full 3D simulations

In this section, we present the results of the simulation in which both the MRI and gravitational instabilities can develop. We include the Fourier components of the gravitational potential up to $m = 8$. The toroidal magnetic field that we add to the equilibrium structure is the same as that described in the previous section. For this calculation, the resolution is $(N_r, N_\phi, N_z) = (128, 64, 128)$ and the azimuthal domain is $[0, \pi]$.

As expected, we observe the simultaneous appearance of MHD turbulence along with the $m = 2$ spiral arm reminiscent of the hydrodynamical calculation. To analyze the angular momentum transport properties, we compare the time evolution of the volume averaged gravitational and Maxwell stress tensors ob-

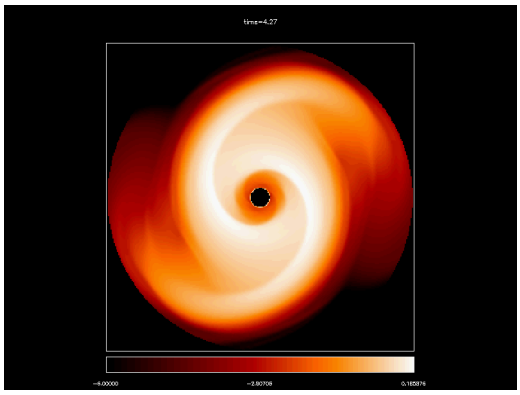

Figure 5. Logarithm of the density in the equatorial plane after 4.27 orbits.

tained in this simulation with that obtained in the runs described above. Note that the gravitational stress tensor is defined by:

$$T_{r\phi}^{grav} = \frac{1}{4\pi G} \int \frac{1}{r} \frac{\partial \Phi_g}{\partial r} \frac{\partial \Phi_g}{\partial \phi} d\tau \,. \tag{4}$$

The left panel of figure 7 shows $T_{r\phi}^{grav}$ as a function of time for this simulation (*dotted line*) and during the hydrodynamical run (*solid line*). We can see that the presence of MHD turbulence decreases the strength of the gravitational stress by a factor of about 2. This result shows that MHD turbulence and the gravitational instability strongly interact with each other. The time evolution of the Maxwell stress is shown on the right panel of figure 7 for the full simulation (*dotted line*) and for the MHD run in an axisymmetric potential (*dashed line*). We see that the Maxwell stress increases when the gravitational instability develops. This appears to be due to the accumulation of the magnetic field along the spiral arms. When the gravitational instability disappears after about 7 orbits (because of a decrease of the mass density), the Maxwell stress goes back to its "turbulent" value.

To test the sensitivity of our results to the initial field topology, we have run the same calculation with an initial poloidal magnetic field. We found the same qualitative results.

5. Conclusions and Perspectives

We have presented here the first global simulations of massive, magnetized disks.

Using 2D axisymmetric numerical simulations, we have shown that the properties of the MRI are similar in self–gravitating and zero mass disks. We observe that these disks quickly develop a dual structure composed of an inner thin disk in Keplerian rotation around the central mass, and a thicker outer torus whose rotation profile is close to a Mestel profile.

We have then used 3D simulations to study the angular momentum transport properties in disks when both MHD turbulence and gravitational instabil-

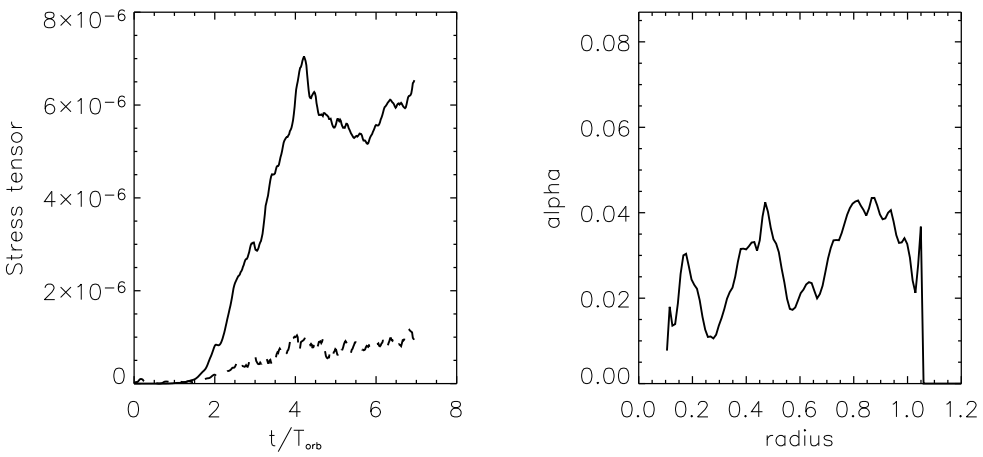

Figure 6. Left panel: time evolution of the Maxwell (*solid line*) and Reynolds (*dashed line*) stress tensor in the MHD run with an axisymmetric gravitational potential. Right panel: radial profile of the α parameter.

ities are present. We have found that the gravitational instability is affected by the presence of the turbulence: the gravitational stress tensor is decreased by roughly a factor of 2 when compared with hydrodynamical simulations. This results in a smaller mass accretion rate toward the central object. Self–gravitating disks may therefore have a longer lifetime than previously thought.

Note that the simulations presented here use an adiabatic equation of state. In this case, all the energy generated in shocks and compression is locally converted into heat. This prevents the formation of bound objects by gravitational collapse. The opposite case would correspond to the use of a locally isothermal equation of state, for which all the energy generated is immediately radiated away. Several authors (Mayer et al. 2002, Rice et al. 2003, Boss 1997 & 1998) have indeed reported gravitational collapse in isothermal calculations of disks, although this issue is still under debate (Pickett et al. 2003). We believe that the presence of MHD turbulence affects the thermal balance in the disk and therefore needs to be included. We are currently performing calculations of isothermal massive and magnetized disks.

References

Balbus,S., Hawley,J., 1991, *ApJ*, 376, 214

Balbus,S., Hawley,J., 1998, *Rev. Mod Phys.*, 70, 1

Boss,A.P., 1997, *Science*, 276, 1836

Boss,A.P., 1998, *ApJ*, 503, 923

Cohl,H., Tohline,J., 1999, *ApJ*, 527, 86

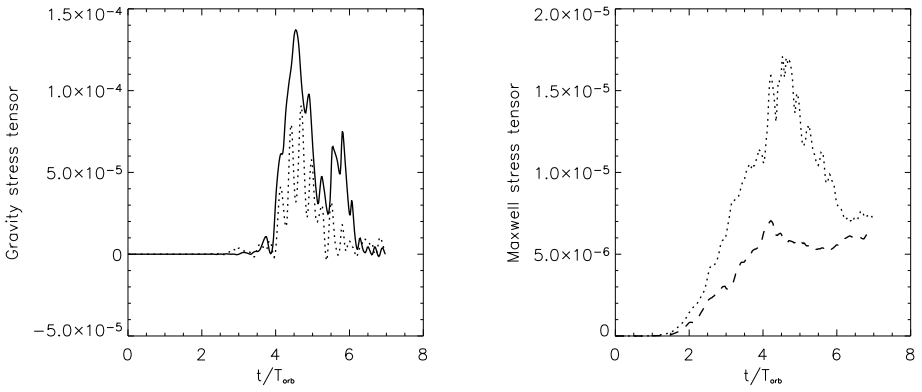

Figure 7. Left panel: time evolution of the gravitational stress tensor in the hydrodynamical run (*solid line*) and in the full simulation (*dotted line*). Right panel: time evolution of the Maxwell stress tensor in the full simulation (*dotted line*) and in the 3D MHD run with an axisymmetric gravitational potential (*dashed line*).

Hawley,J., Stone,J., 1995, *Comput. Phys. Commun.*, 89, 127

Hawley,J., 2000, *ApJ*, 528, 462

Hachisu,I., 1986, *ApJS*, 62, 461

Hirsch,C., *Numerical Computation of Internal and External Flows - Volume 1, Fundamentals of Numerical Discretization.* Wiley (1988)

Laughlin.G, Korchagin,V., Adams,F.C., 1998, *ApJ*, 504, 945

Mayer,L., Quinn,T., Wadsley,J., Stadel,J., 2002, *Science*, 298

Stone,J., Norman,M., 1992a, *ApJS*, 80, 753

Stone,J., Norman,M., 1992b, *ApJS*, 80, 791

Steinacker,A., Papaloizou,J., 2002, *ApJ*, 571, 413 Press,W.H.,

Rice, W. K. M., Armitage, P. J., Bate, M. R., Bonnell, I. A., 2003, MNRAS, 339, 1025